Nano World Journal

https://doi.org/10.17756/nwj.2023-s2-014

Research Article

Open Access

Synthesis of Fluorapatite-tetracalcium Phosphate Mixtures from Electric Arc Furnace Slag

H. Agourrame*, F. Ouzoun, H. Ez-zaki, N. Khachani and A. Diouri*

Faculté des Sciences, Université Mohammed V de Rabat, Avenue Ibn Battouta, BP 1014, Laboratoire de Chimie Appliquée des Matériaux, Rabat, Morocco

***Correspondence to:**
H. Agourrame
Faculté des Sciences,
Université Mohammed V de Rabat,
Avenue Ibn Battouta, BP 1014,
Laboratoire de Chimie Appliquée des Matériaux,
Rabat, Morocco.
E-mail: hind.agourrame@gmail.com

A. Diouri
Faculté des Sciences,
Université Mohammed V de Rabat,
Avenue Ibn Battouta, BP 1014,
Laboratoire de Chimie Appliquée des Matériaux,
Rabat, Morocco.
E-mail: a.diouri@um5r.ac.ma

Received: July 25, 2023
Accepted: September 20, 2023
Published: September 22, 2023

Citation: Agourrame H, Ouzoun F, Ez-zaki H, Khachani N, Diouri A. 2023. Synthesis of Fluorapatite-tetracalcium Phosphate Mixtures from Electric Arc Furnace Slag. *NanoWorld J* 9(S2): S81-S86.

Published by United Scientific Group

Abstract

The steelmaking process results in the by-product formation of electric arc furnace slag (EAFS). Slag is recovered at two different stages of the steelmaking process, the first recovery is black and the second is white mainly consisting of SiO_2, CaF_2, and CaO. Steel slag is a solid waste produced in the metallurgical industry. The present research focuses on the white slag from SONASID-Jorf steel in Morocco for preparation of fluorapatite ($Ca_5(PO_4)_3F$)-tetracalcium phosphate ($Ca_4(PO_4)_2O$; TTCP) phases. These phases were successfully synthesized by activated slag with alkali activator NaOH (Sodium hydroxide) and using a wet precipitation method with molar ratio of Ca/P = 1.67. X-ray diffraction (XRD), Fourier transform infrared (FTIR) spectroscopy measurement, and scanning electron microscopy (SEM) analysis techniques were performed on the samples to characterize the mineralogical and microstructural properties. The characterization of the developed phases indicates the formation of mixtures of dicalcium silicate (Ca_2SiO_4) with reinhardbraunsite ($Ca_5((SiO)_4)_2OH_2$) and cuspidine ($Ca_4Si_2F_2O_7$) phases in the white slag activated with alkali activator NaOH. Moreover, indicates the formation of the fluorapatite-TTCP phases synthesized by wet precipitation method. The micrographs obtained by SEM show the morphology of rounded particles in the form attributed to fluorapatite phase and like woven nets attributed to tetracalcium phosphate.

Keywords

Blast furnace slag, Fluorapatite, Tetracalcium phosphate, Reinhardbraunsite

Introduction

Blast furnace slag (BFS) is an industrial by product, rich in calcium, silicon, and aluminum components. About 400 million tons of slags are produced annually worldwide as a by-product of the steelmaking process [1, 2]. Several slag types derived from steel production may be listed: BFS, electric arc-furnace oxidizing slag, ladle-furnace basic slag, etc. According to the World Steel Association, world crude steel production has increased from 849 Mt in 2000 [1] to 1690 Mt for the year 2018 [3]. EAFS is a by-product of the steelmaking industry, generated after the melting and the primary acid refining of liquid steel. Its chemical composition is based on its content of calcium, iron, and silicon oxides in a global amount of over 80%, aluminum, magnesium, manganese, and phosphorus oxides are also present [4]. The main compounds of EAFS, according to the scientific literature, are single and complex calcium silicates (containing aluminum or magnesium) and single and complex iron-based oxides (containing calcium, magnesium, chromium, manganese, among others) which are in a liquid state above 1500 °C, aided by fluxes such as CaF_2, which solidify at under 1200 °C [5]. However, EAFS corresponds to metal oxides trapped in fluxes such as lime and dolomite [6]. The easiness of activation and the hydration of the slags depend

mainly upon the mineralogical composition and fineness of the slag and on the type of the alkaline activator used [7]. Murri et al. demonstrated that it is possible to produce granulated BFS based geopolymeric binder using NaOH combined with sodium silicate as alkaline activators [8]. On the other hand, the activation of BFS using alkali, specifically NaOH, resulted in the formation of C-S-H gels and reinhardbraunsite [9]. This latter compound has been synthesized firstly by Buckle and Taylor from tricalcium silicate and water under hydrothermal conditions above 700 °C [10]. According to recent studies, the mineral reinhardbraunite has been found to undergo decomposition when subjected to standard conditions at temperatures above 650 °C [11]. Peak appeared at 30.9° and 31.4° corresponded to the crystalline phase of reinhardbraunsite [12]. A hydroxyapatite-zeolite composite material was successfully synthesized from steel slag using particular chemical reagents, H_3PO_4 and NaOH, utilizing the inherent chemical composition of steel slag [13]. Therefore, mixtures of BFS and fluorite tailing are suitable for diopside-based glass-ceramics. Research demonstrated had fluorapatite-based glass-ceramics could be obtained from blast furnace slag and fluorite tailing, which exhibit excellent bioactive and mechanical properties [14]. Fluorapatite with the chemical formula of $Ca_5(PO_4)_3F$ is one of the apatite families with the most stable phase, least soluble in the physiological condition of human body fluid, with the hardest characteristics [15]. Fluorapatite has recently attracted considerable attention because the presence of fluoride enhances the biodegradability and compressive strength and stimulates the formation of bone tissues [16]. Moreover, hydroxyapatite and fluoroapatite have essentially the same molecular structure as they only differ by the OH or F ion that is located within the hexagonal pattern [17]. In laboratories, it can be synthesized by reactions in solid state, co-precipitation route, hydrothermal methods, sol-gel process, wet chemical precipitation method, or sonochemistry method [18]. Are remarkably used for orthopaedics and orthodontic applications owing to their excellent biocompatibility, osseointegration and osteoconductive properties [19]. Moreover, Chen et al. prepared fluorapatite-diopside glass-ceramics with a microhardness of 7.36 GPa from BFS (40 mass%) and fluorite tailings (60 mass%) [20]. TTCP ($Ca_4(PO_4)_2O$, mineralogical name: hilgenstockite) was first described 1883 by Hilgenstock [21] as tabular crystals as a component of the basic and phosphate-rich slag obtained during steel production according to the Thomas process. The slag was extensively used as fertilizer in the 19th and 20th centuries, owing to the higher solubility of the compounds TTCP and $Ca_3(PO_4)_2$.Ca_2SiO_4 compared with natural phosphate sources such as apatite minerals [22, 23]. TTCP, a major compound of cement in dentistry was prepared through different solid-state reactions at 1300 and 1350 °C [10]. The steel slag with basicity larger than 1.6 is thought to contain certain content of dicalcium silicate (C_2S) and tricalcium silicate (C_3S) which endow steel slag cementitious properties [24]. The evolution of dicalcium silicate β to γ allotropic form. Due to the presence of P_2O_5 and other β-phase stabilizers in the arc furnace slag, this reaction is not frequent [25]. In this study, the simultaneous synthesis of fluorapatite-TTCP composites material from EAFS activated slag with alkali activator NaOH and using a wet precipitation of Si, Ca, CaF_2 and Ca components as fluorapatite and TTCP, respectively. With molar ratio of Ca/P = 1.67. The synthesis was performed using phosphoric acid as a solvent and also as a phosphorous source of fluorapatite. Phosphoric acid was employed with the aim of once dissolving steel slag and facilitating the subsequent chemical reaction. The synthesis mechanism was investigated in detail by XRD, SEM, and FTIR spectroscopy.

Materials and Method

The syntheses of fluorapatite and TTCP phases in this study were conducted as follows: To enhance dissolution performance, EAFS was ground and sieved using a < 40µm sieve prior to synthesis. Initially, the obtained powder was activated using a mixture of NaOH of ratio S/L = 2. The activated samples, referred to as SWN (White slag), were then heated in a ceramic container at 600 °C for 90 minutes. After cooling, the product was crushed. Afterward, a 5.0 g of the fusion product powder (SWN) was taken and dissolved in 30 ml of 2.0 mol/L NaH_2PO_4 aqueous solution until homogenized. Once dissolution is completed, another 50 ml of 3.0 mol/L NaOH aqueous solution was added drop by drop into the above suspension. It should be noted that the Ca/P molar ratio of the suspension was fixed at 1.7, the obtained slurry was vigorously stirred for 2 h at 100 °C, subsequently aged at the same temperature for a certain time without stirring to achieve crystallization. At the end of the process the solid phase was collected by filtration, washed several times with distilled water, and then dried at 80 °C. Sample prepared with the NaH_2PO_4 are named respectively SWNP (White slag). Fluorapatite with nanoproperties.

Results and Discussion

FTIR spectroscopy

The chemical composition of the BFS used in the present study was investigated by X-ray fluorescence spectroscopy, results are listed in table 1. The slag was mainly composed of CaO, Al_2O_3, MgO and SiO_2 components, which are needed to synthesize fluorapatite and TTCP.

Table 1: Chemical composition of the white slag sample Sonasid-Jorf steel in Morocco.

Oxides	SW (< 40µm)
SiO_2	16.60
Al_2O_3	1.85
Fe_2O_3	1.27
CaO	37,99
MgO	5.21
SO_3	1.09
K_2O	0
TiO_2	0.14
MnO	0.17
P_2O_5	0.01
SrO	0.016
LOI	34.65

X-ray diffraction

Figure 1 shows the XRD diagrams of the white slag. The analyses show that the main crystallized phases identified in the white slag (SW) are dicalcium silicate (Ca_2SiO_4, PDF# 99-101-2641), Calcium fluoride (CaF_2, PDF# 99-200-0043), Magnesium oxide (MgO, PDF# 99-200-0053), Aluminum oxide (Al_2O_3, PDF# 99-200-0440), and Rankinite ($Ca_3Si_2O_7$, PDF# 99-101-1835). Furthermore, the presence of dicalcium silicate (C_2S) is the preferred phase in slag from the observed peak intensity, which shows that the C_2S phase is the main constituent in slag [26].

Figure 2 shows the XRD patterns of white slag alkali activated with NaOH. The analyses show that the dicalcium silicate (β-Ca_2SiO_4, PDF# 99-101-2811) phase identified in the white slag (SWN) of the monoclinic crystal system metastable at room temperature [27]. It is clear that the crystallinity of the synthesized composite samples was influenced by the NaOH concentration of the initial mixture. The SWN spectre consists of the reinhardbraunsite ($Ca_5((SiO)_4)_2OH_2$, PDF# 99-101-1430) and cuspidine ($Ca_4Si_2F_2O_7$, PDF# 99-200-4323) phases. Reinhardbraunsite crystallizes in monoclinic system, P21/a, with a = 11.458(2), b = 5.052(1), c = 8.840(2) A [28]. Reinhardbraunsite crystals extended along the [0 0 1] direction. The basic unit of reinhardbraunsite based on the tetrahedral coordination cation Si = 2 is combined with Ca = 5 [29]. The XRD pattern of BFS activated by 1.5 wt.% NaOH at 80 °C showed that the BFS hydration reaction produced reinhardbraunsite [9]. Minerals belonging to the cuspidine group have the general stoichiometry $M_4(Si_2O_7)X_2$ (M = Divalent cation, X = OH, F, O), with $Ca_4(Si_2O_7)(OH, F)_2$ being the archetype compound. The cuspidine structure can be described as built up of chains of edge-sharing MO7/MO8 polyhedral running parallel to axis (in the P21/c space group), the tetrahedral disilicate groups (Si_2O_7) interconnect with these ribbons through the vertices [30]. The XRD pattern (SWNP) for 2 h of aging showed several diffraction peaks assignable to fluorapatite ($Ca_5(PO_4)_3F$, PDF#99-100-7812) and TTCP ($Ca_4(PO_4)_2O$, PDF#99-100-8735) phases in the white slag. Fluorapatite has the same crystal structure as hydroxyapatite, except that the OH- group is replaced by an F atom. The F atom is smaller, so the crystal structure of fluorapatite (lattice constant a = b = 9.368 Å, c = 6.884 Å) is more compact than that of hydroxyapatite (lattice constant a = b = 9.425 Å, c = 6.884 Å) [31]. The fluorapatite material crystallizes in the hexagonal P63/m space group with ten Ca^{2+} ions placed in two different crystallographic symmetry positions: Ca1 (4f) and Ca2 (6h) [32]. In the recent study, the presence of characteristic peaks of the TTCP phase was demonstrated. This phase was found crystallize in the monoclinic unit cell, with a space group of P21. The unit cell parameters were determined to be a = 7.023 Å, b = 11.986 Å, c = 9.473 Å, and β = 90.90 at 25 °C [33].

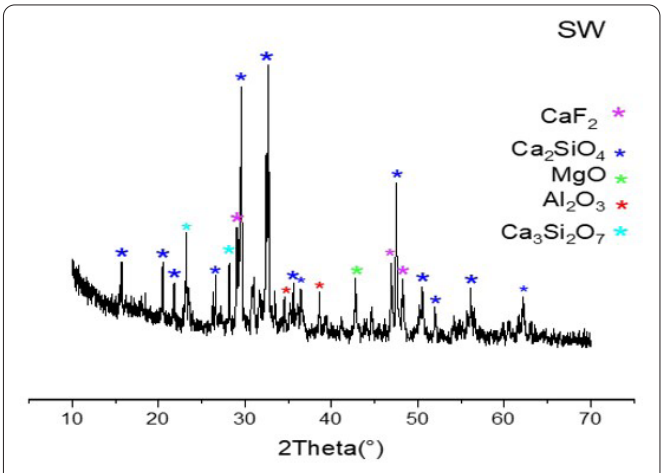

Figure 1: XRD spectra of white slag sample.

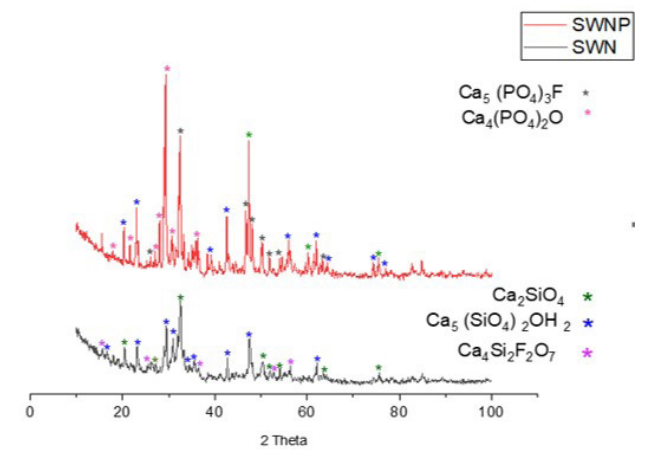

Figure 2: X-ray diffractogram of SWN and SWNP powders.

FTIR spectroscopy

The FTIR spectrum of the (SWN-SWNP) powders is presented in figure 3. The majority of the detected absorption bands correspond to the polymorph of the dicalcium silicate α-Ca_2SiO_4 are located around 800 - 1000 cm^{-1} [34]. The bands of the white slag (SWN) in the figure 3 shows a defined the absorption bands of cuspidine can be grouped in several kinds of bands corresponding to the stretching vibrations of the [Si-O_4]- tetrahedra. These groups are observed in the 1220 - 760 cm^{-1} range. The bands observed around 653, 555 - 510 and 430 cm^{-1} can be attributed to, [SiF_6]$_2$-octahedral complexes, Si-O bonding, and Ca-O, respectively [35]. We notice that the existence of the PO_4^{3-} of fluorapatite represented by the O-P-O

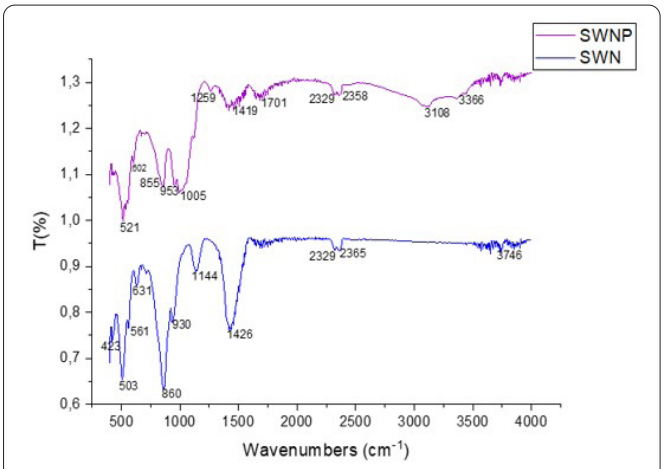

Figure 3: FTIR spectrum of SWN and SWNP powders.

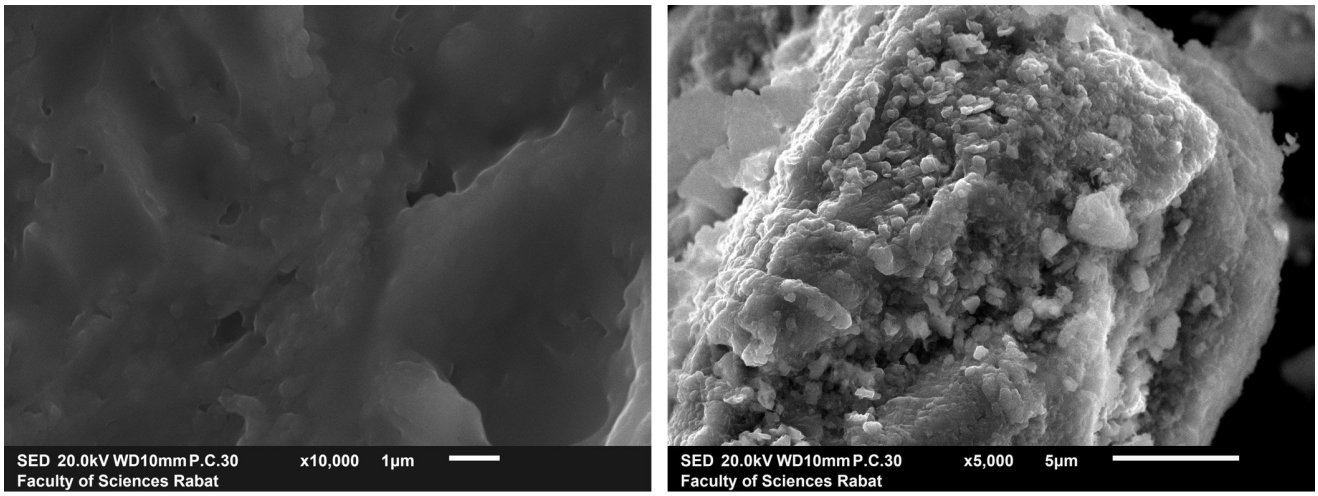

Figure 4: SEM image of **(a)** SWN at x5000 and **(b)** SNBP at x10000.

bending vibrations around wavenumber 603 cm^{-1} [36]. The absorption peak located at 603 cm^{-1}, were assigned to the υ4 vibration mode of PO_4^{3-} [37]. The bands between 400 and 650 cm^{-1} are due to the deformation of the O-P-O angle [38]. Very broad bands for molecular water at about 3300 - 3600 cm^{-1}(OH stretch) [28]. Finally, two bands relating to vibration of the adsorbed water in apatite lattice could be noticed as a broad peak between 3600 and 3000 cm^{-1} [29].

Scanning electron microscopy

SEM (JSM-7000F FE-SEM) is used to study the morphology of samples and obtain information on crystal shape, size, and grain texture. SEM micrographs of the SBN sample is shown in figure 4a. While in the SWN sample is shown in figure 4 the aggregated small particles were reinhardbraunsite, also known as calcio-chondrodite [38]. They show the presence of rod-bulky crystals [39]. And long needle crystals and bulky crystals [40] indicate the presence of reinhardbraunsite. Cuspidine together with larnite occurs as a fine-grained aggregate in intermediate zones of nodules and separate crusts [41]. SEM micrographs of the SWNP samples shown in figure 4b. They show the morphology like woven nets which can be attributed to TTCP [42]. The spherical shape grains apparent above this woven [43]. However, these rounded particles can be attributed to fluorapatite phase [44].

Conclusion

In this study, fluorapatite-TTCP composites materials were successfully synthesized from steel slag using particular chemical reagents, NaH_2PO_4 and NaOH. The results of this study can be summarized the following major conclusions: XRD results showed that reinhardbraunsite and cuspidine phases could be clearly observed with activator NaOH. The TTCP and fluorapatite phases synthesized by wet precipitation method give morphology like woven nets particles and the fractured clear cracks. Fluorapatite-TTCP were successfully synthesized from EAFS with a fusion method involving alkaline fusion and a wet precipitation method treatment in this research. The identified composites have good prospects for wastewater treatment.

Acknowledgments

None.

Conflict of Interest

None.

References

1. Turkdogan ET. 1984. Physicochemical aspects of reactions in ironmaking and steelmaking processes. *Trans Iron Steel Inst Japan* 24(8): 591-611. https://doi.org/10.2355/isijinternational1966.24.591
2. Proctor DM, Fehling KA, Shay EC, Wittenborn JL, Green JJ, et al. 2000. Physical and chemical characteristics of blast furnace, basic oxygen furnace, and electric arc furnace steel industry slags. *Environ Sci Technol* 34(8): 1576-1582. https://doi.org/10.1021/es9906002
3. Shi C, Wang X, Zhou S, Zuo X, Wang C. 2022. Mechanism, application, influencing factors and environmental benefit assessment of steel slag in removing pollutants from water: a review. *J Water Process Eng* 47: 102666. https://doi.org/10.1016/j.jwpe.2022.102666
4. Alsheyab MA, Khedaywi TS. 2013. Effect of electric arc furnace dust (EAFD) on properties of asphalt cement mixture. *Resour Conserv Recycl* 70: 38-43. https://doi.org/10.1016/j.resconrec.2012.10.003
5. Luxán MP, Sotolongo R, Dorrego F, Herrero E. 2000. Characteristics of the slags produced in the fusion of scrap steel by electric arc furnace. *Cem Concr Res* 30(4): 517-519. https://doi.org/10.1016/S0008-8846(99)00253-7
6. Lee S, Min DJ. 2018. Viscous behavior of FeO-bearing slag melts considering structure of slag. *Steel Res Int* 89(8): 1800055. https://doi.org/10.1002/srin.201800055
7. Rađenović A, Malina J, Sofilić T. 2013. Characterization of ladle furnace slag from carbon steel production as a potential adsorbent. *Adv Mater Sci Eng* 2013: 198240. https://doi.org/10.1155/2013/198240
8. Latorrata S, Balzarotti R, Adami MI, Marino B, Mostoni S, et al. 2021. Wastewater treatment using alkali-activated-based sorbents produced from blast furnace slag. *Appl Sci* 11(7): 2985. https://doi.org/10.3390/app11072985

9. Dong J, Li C, Liu H, Zhang L, Liu J. 2019. Investigating the mechanical property and reaction mechanism of geopolymers cement with red Pisha Sandstone. *Constr Build Mater* 201: 641-650. https://doi.org/10.1016/j.conbuildmat.2018.12.202
10. Cámara F, Gagne OC, Uvarova Y, Belakovskiy DI. 2016. New mineral names. *Am Min* 101(9): 2123-2131. https://doi.org/10.2138/am-2016-NMN101916
11. Roßkopf C, Afflerbach S, Schmidt M, Görtz B, Kowald T, et al. 2015. Investigations of nano coated calcium hydroxide cycled in a thermochemical heat storage. *Energy Convers Manag* 97: 94-102. https://doi.org/10.1016/j.enconman.2015.03.034 +
12. Hamzah HK, Huseien GF, Asaad MA, Georgescu DP, Ghoshal SK, et al. 2021. Effect of waste glass bottles-derived nanopowder as slag replacement on mortars with alkali activation: durability characteristics. *Case Stud Constr Mater* 15: e00775. https://doi.org/10.1016/j.cscm.2021.e00775
13. Haha MB, Lothenbach B, Le Saout GL, Winnefeld F. 2011. Influence of slag chemistry on the hydration of alkali-activated blast-furnace slag—part I: effect of MgO. *Cem Concr Res* 41(9): 955-963. https://doi.org/10.1016/j.cemconres.2011.05.002
14. Shimazaki H, Miyawaki R, Yokoyama K, Matsubara S, Bunno M. 2008. Occurrence and new data of dellaite from the Akagane mine, Japan. *J Min Petrol Sci* 103(6): 385-389. https://doi.org/10.2465/jmps.080214
15. Li C, Li X, Yu Y, Zhang Q, Li L, et al. 2022. A novel conversion for blast furnace slag (BFS) to the synthesis of hydroxyapatite-zeolite material and its evaluation of adsorption properties. *J Ind Eng Chem* 105: 63-73. https://doi.org/10.1016/j.jiec.2021.08.017
16. Khanday WA, Hameed BH. 2018. Zeolite-hydroxyapatite-activated oil palm ash composite for antibiotic tetracycline adsorption. *Fuel* 215: 499-505. https://doi.org/10.1016/j.fuel.2017.11.068
17. Huang J, Liu T, Zhang Y, Hu P. 2022. Internal coordination of vanadium industrial waste—preparation of hydroxyapatite and fluorine wastewater purification. *J Water Process Eng* 49: 103041. https://doi.org/10.1016/j.jwpe.2022.103041
18. Nikolić I, Đurović D, Tadić M, Radmilović VV, Radmilović VR. 2020. Adsorption kinetics, equilibrium, and thermodynamics of Cu^{2+} on pristine and alkali activated steel slag. *Chem Eng Commun* 207(9): 1278-1297. https://doi.org/10.1080/00986445.2019.1685986
19. Ryu GU, Kim GM, Khalid HR, Lee HK. 2019. The effects of temperature on the hydrothermal synthesis of hydroxyapatite-zeolite using blast furnace slag. *Materials* 12(13): 2131. https://doi.org/10.3390/ma12132131
20. Abukhadra MR, Dardir FM, Shaban M, Ahmed EA, Soliman MF. 2018. Superior removal of Co^{2+}, Cu^{2+} and Zn^{2+} contaminants from water utilizing spongy Ni/Fe carbonate–fluorapatite; preparation, application and mechanism. *Ecotoxicol Environ Safety* 157: 358-368. https://doi.org/10.1016/j.ecoenv.2018.03.085
21. Mobasherpour I, Salahi E, Pazouki M. 2011. Removal of divalent cadmium cations by means of synthetic nano crystallite hydroxyapatite. *Desalination* 266(1-3): 142-148. https://doi.org/10.1016/j.desal.2010.08.016
22. Chang KL, Huang CT, Huang W, Liu YC. 2008. Investigations of microstructure and phosphorus distribution in BOF slag. *China Steel Tech* Rep 21: 1-6.
23. Midgley CM. 1952. The crystal structure of β dicalcium silicate. *Acta Cryst* 5(3): 307-312. https://doi.org/10.1107/S0365110X52000964
24. Tantawy MA, Shatat MR, El-Roudi AM, Taher MA, Abd-El-Hamed M. 2014. Low temperature synthesis of belite cement based on silica fume and lime. *Int Sch Res Notices* 2014: 873215. https://doi.org/10.1155/2014/873215
25. Kurashina K, Kurita H, Kotani A, Takeuchi H, Hirano M. 1997. *In vivo* study of a calcium phosphate cement consisting of α-tricalcium phosphate/dicalcium phosphate dibasic/tetracalcium phosphate monoxide. *Biomaterials* 18(2): 147-151. https://doi.org/10.1016/S0142-9612(96)00173-1
26. Zhang S, Zhu N, Mao F, Zhang J, Huang X, et al. 2021. A novel strategy for harmlessness and reduction of copper smelting slags by alkali disaggregation of fayalite (Fe_2SiO_4) coupling with acid leaching. *J Hazard Mater* 402: 123791. https://doi.org/10.1016/j.jhazmat.2020.123791
27. Zhao X, Liu Q, Yang J, Zhang W, Wang Y. 2018. Sintering behavior and mechanical properties of mullite fibers/hydroxyapatite ceramic. *Materials* 11(10): 1859. https://doi.org/10.3390/ma11101859
28. Fleet ME, Liu X. 2008. Accommodation of the carbonate ion in fluorapatite synthesized at high pressure. *Am Min* 93(8-9): 1460-1469. https://doi.org/10.2138/am.2008.2786
29. Sharifnabi A, Fathi MH, Yekta BE, Hossainalipour M. 2014. The structural and bio-corrosion barrier performance of Mg-substituted fluorapatite coating on 316L stainless steel human body implant. *Appl Surf Sci* 288: 331-340. https://doi.org/10.1016/j.apsusc.2013.10.029
30. Morán-Ruiz A, Wain-Martin A, Orera A, Sanjuán ML, Larranaga A, et al. 2019. Synthesis of new $Ln_4(Al_2O_6F_2)O_2$ (Ln= Sm, Eu, Gd) phases with a cuspidine-related structure. *IUCrJ* 6(1): 128-135. https://doi.org/10.1107/S205225251801744X
31. Xie J, Zhang Q, Mao S, Li X, Shen Z, et al. 2019. Anisotropic crystal plane nature and wettability of fluorapatite. *Appl Surf Sci* 493: 294-307. https://doi.org/10.1016/j.apsusc.2019.06.195
32. Milojkov DV, Sokić M, Radosavljević-Mihajlović A, Stanić VD, Manojlović V, et al. 2021. Influence of Pr^{3+} and CO_3^{2-} ions coupled substitution on structural, optical and antibacterial properties of fluorapatite nanopowders obtained by precipitation. *Metals* 11(9): 1384. https://doi.org/10.3390/met11091384
33. Moseke C, Gbureck U. 2010. Tetracalcium phosphate: synthesis, properties and biomedical applications. *Acta Biomater* 6(10): 3815-3823. https://doi.org/10.1016/j.actbio.2010.04.020
34. Mollah MY, Tsai YN, Hess TR, Cocke DL. 1992. An FTIR, SEM and EDS investigation of solidification/stabilization of chromium using portland cement Type V and Type IP. *J Hazard Mater* 30(3): 273-283. https://doi.org/10.1016/0304-3894(92)87004-Y
35. Chen H, Sun Q, Zhang J, Sheng J. 2022. Effect of MgF_2 addition on sinterability and mechanical properties of fluorapatite ceramic composites fabricated by wollastonite and phosphate glass. *Ceram Int* 48(14): 20400-20408. https://doi.org/10.1016/j.ceramint.2022.03.325
36. Kheradmandfard M, Fathi MH. 2013. Fabrication and characterization of nanocrystalline Mg-substituted fluorapatite by high energy ball milling. *Ceram Int* 39(2): 1651-1658. https://doi.org/10.1016/j.ceramint.2012.08.007
37. Ghica D, Vlaicu ID, Stefan M, Maraloiu VA, Joita AC, et al. 2019. Tailoring the dopant distribution in ZnO: Mn nanocrystals. *Sci Rep* 9(1): 6894. https://doi.org/10.1038/s41598-019-43388-z
38. Wei T, Cheng X, Liu H, Zhang H, Zhang L, et al. 2022. Crystallization of tricalcium silicate blended with different silica powder dosages at high temperature. *Constr Build Mater* 316: 125884. https://doi.org/10.1016/j.conbuildmat.2021.125884
39. Dai T, Liu T, Jiang G, Qu B, Zheng S. 2022. Evaluation of microstructural and mechanical properties of silica-enriched oil well cement pastes in steam injection wells. *SSRN* 4048736. http://dx.doi.org/10.2139/ssrn.4048736
40. Yanagisawa K, Hu X, Onda A, Kajiyoshi K. 2006. Hydration of β-dicalcium silicate at high temperatures under hydrothermal conditions. *Cem Concr Res* 36(5): 810-816. https://doi.org/10.1016/j.cemconres.2005.12.009
41. Leng M, Lai F, Li J. 2018. Effect of cooling rate on phase and crystal morphology transitions of CaO–SiO_2-based systems and CaO–Al_2O_3-based systems. *Materials* 12(1): 62. https://doi.org/10.3390/ma12010062
42. Zhang X, Zhou J, Cheng J, Zhu J, He D. 2020. ZnO-assisted coating of tetracalcium phosphate/gelatin on the polyethylene terephthalate woven nets by atomic layer deposition. *e-Polymers* 20(1): 85-91. https://doi.org/10.1515/epoly-2020-0010

43. Manafi S, Mirjalili F, Reshadi R. 2019. Synthesis and evaluation of the bioactivity of fluorapatite–45S5 bioactive glass nanocomposite. *Prog Biomater* 8(2): 77-89. https://doi.org/10.1007/s40204-019-0112-y

44. Altaie A, Bubb N, Franklin P, German MJ, Marie A, et al. 2020. Development and characterisation of dental composites containing anisotropic fluorapatite bundles and rods. *Dental Mater* 36(8): 1071-1085. https://doi.org/10.1016/j.dental.2020.05.003